Astronomy & Astrophysics manuscript no. AlCir2_draft_v12c
March 29, 2020

New BRITE-Constellation⋆ observations of the roAp star α Cir

W. W. Weiss[1†], H.-E. Fröhlich[2], T. Kallinger[1], A. Pigulski[3 † ⋄], R. Kuschnig[1,4 † ⋄], A. Popowicz[5 † ⋄], D. Baade[99†], D. Buzasi[99], O. Kochukhov[99], A. F. J. Moffat[99 † ⋄], K. Zwintz[99†], O. Koudelka[4†], and BEST (tbd)

[1] University of Vienna, Institute for Astrophysics, Vienna, Austria; e-mail: werner.weiss@univie.ac.at
[2] Kleine Strasse 9, D-14482 Potsdam;
[3] Astronomical Institute, University of Wrocław, Poland;
[4] Institut fuer Kommunikationsnetze und Satellitenkommunikation, Graz University of Technology, Austria;
[5] Silesian University of Technology, Department of Electronics, Electrical Engineering and Microelectronics, Poland;
[6] * to be put in proper sequence: *
[7] Universität Innsbruck, Institute for Astro- and Particle Physics, Technikerstrasse 25, A-6020 Innsbruck;
[8] Department of Chemistry and Physics, Florida Gulf Coast University, USA;
[9] Department of Physics and Astronomy, Uppsala University, Sweden;
[10] European Organisation for Astronomical Research in the Southern Hemisphere (ESO), Germany;
[11] Dept. de physique, Université de Montréal;

Received ; accepted

ABSTRACT

Context. Chemically peculiar (CP) stars with a measurable magnetic field build the group of mCP stars. Many of them pulsate and they are also members of the group of rapidly oscillating Ap (roAp) stars. α Cir is the brightest member of the latter and allows therefore application of challenging techniques, like interferometry, very high temporal and spectral resolution photometry and spectroscopy in a wide wavelength range, which can provide unique information about the structure and evolution of a star.
Aims. Based on new photometry from BRITE-Constellation, obtained with blue and red filters, we attempt to determine the surface spot structure of α Cir, investigate the pulsation frequency spectrum and put the new observations in context of previous investigations.
Methods. The photometric surface imaging and frequency analyses use Bayesian techniques .
Results. BRITE-Constellation photometry obtained from 2014 to 2016 is put in context of space photometry obtained by WIRE, SMEI, and TESS. This allows for a critical assessment of rotation, surface features (spots) and main pulsation frequencies using Bayesian techniques and discussing advantages and problems of the last.

Key words. Space photometry – Stars: chemically peculiar – Starspots – Pulsation – HD 128898, α Cir

1. Introduction

α Cir is a well-known and well-observed rapidly oscillating chemically peculiar (roAp) star with a main pulsation period of 6.8 min (Kurtz & Balona (1984)), and has a mean quadratic magnetic field of 4 kΓ to 7 kΓ (Mathys 2017) and rotates with $P_{\rm rot} = 4.478$ d. Such a large quadratic field, however, is controversial as it indicates a very strong field, which is not found by any other technique (Bruntt et al. 2009). We have summarised already in Weiss et al. (2016, hereafter Paper I), past investigations of α Cir and provided references. Striking differences between the rotation light curves in the red and blue filter observations with BRITE-Constellation (Weiss et al. 2014) were discussed which called for clarification.

The data needed for this clarification were obtained by three of the five BRITE-Constellation satellites in 2016 which are the subject of this paper. In addition we analyse WIRE data from 2006 and 2007 (Bruntt et al. 2009), and data which SMEI obtained from 2003 to 2010 (Jackson et al. 2004; Tarrant et al. 2008), and which cover the two last WIRE seasons. Finally, we address also TESS data (Ricker et al. 2015), which were obtained in 2019. The large time base of almost 20 years of observing α Cir with various space missions allows us to discuss rotation and pulsation, with an excursion to inherent problems of photometric surface imaging using Bayesian technique in order to locate surface spots. This technique has two main advantages: (i) parameter estimation with the Bayesian technique provides credibility regions from the data alone and (ii) it allows us to rank the various spot models according to their evidence.

Concerning pulsation properties, the dependency of amplitude and phase of the dominant frequency f_1 on the rotation phase of α Cir, addressed in Paper I, was another challenge for the 2016 BRITE photometry. Merging the results with space photometry obtained by WIRE, SMEI, and TESS helped to improve the accuracy significantly. With a much better signal-to-noise (S/N) of the new red and blue 2016 BRITE data, we address also other frequencies mentioned in Bruntt et al. (2009), and in Paper I.

⋆ Based on data collected by the BRITE Constellation satellite mission, designed, built, launched, operated and supported by the Austrian Research Promotion Agency (FFG), the University of Vienna, the Technical University of Graz, the University of Innsbruck, the Canadian Space Agency (CSA), the University of Toronto Institute for Aerospace Studies (UTIAS), the Foundation for Polish Science & Technology (FNiTP MNiSW), and National Science Centre (NCN).
† Member of the BRITE Executive Science Team (BEST).
⋄ Member of the Photometry Tiger Team (PHOTT).

Table 1. Effective wavelengths of the space photometers BAb (BRITE-Austria), BLb (BRITE-Lem), UBr (Uni-BRITE), BTr (BRITE-Toronto), SMEI, WIRE, TESS and their band widths.

	λ (nm)	band width (nm)
BAb & BLb	425	55
UBr & BTr	605	145
WIRE	≈ 600	≈ 380
SMEI	630	≈ 600
TESS	≈ 800	≈ 400

2. Space data and reduction

A basic overview of the BRITE data and their reduction is given already in Paper I describing the status of 2015. As α Cir was observed by different satellites at different epochs, the various data sets exhibit individual peculiarities which we address in the following together with the applied procedures.

The effective wavelengths of the various satellite's passbands were determined by using the filter values and a synthetic spectrum with $T_{\rm eff}$ = 7 500 K, $\log g = 4.1$, and chemical composition, in accordance to what Kochukhov et al. (2009) had determined for α Cir (see Table 1).

2.1. BRITE-Constellation

α Cir was observed in 2014 for 146 days during the commissioning phase of BRITE-Constellation (Weiss et al. 2014). The analysis of these data is presented in Paper I which contains a first attempt at a photometric surface imaging of α Cir in blue and red colours, based on Bayesian techniques and using the rotation period of 4.4790 days, determined by Kurtz et al. (1994).

The star was observed again in the 15-CruCar-I-2016 field from February 4, to July 22, 2016, by three of the five operational nanosatellites, which provided a total of 163 433 photometric measurements from BTr, BAb, and BLb (see Tab. 2) and which are the basis for the present investigation. Each satellite obtained 10 to 30 measurements per satellite orbit (about 101 min) with a typical sampling of 20 s and exposure time of 1 s. For our Bayesian surface imaging, however, we use the average magnitude during one orbit of the respective BRITE satellite, after carefully removing instrumental effects. This broad binning ensures that the brightness variation due to stellar oscillations (less then 2 mmag in the blue and even less in the red filter) cancels out (see Fig. 1). The much larger noise level of the blue data (BAb and BLb) compared to the red data (BTr) is evident. Fortunately, the amplitudes are larger in the blue.

Table 2. 2016 observations of α Cir by BRITE-Constellation: BAb (BRITE-Austria), BLb (BRITE-Lem), and BTr (BRITE-Toronto).

BRITE	filter	# of data points	start dd.mm.yyyy	end dd.mm.yyyy
BAb	blue	29395	04.02.2016	27.05.2016
BLb	blue	48522	03.03.2016	15.07.2016
BTr	red	85516	11.02.2016	22.07.2016

The pipeline outlined by Popowicz (2016) and Popowicz et al. (2017) was used to process the raw images from the satellites. While the pipeline accounts for technical issues typical for the BRITE photometry, such as hot pixels (Pablo et al. 2016), the extracted photometry remains affected by systematic instrumental effects. These systematics, like CCD temperature drifts and position of the star's point spread function (PSF), are identified and removed via decorrelation, similar to that outlined by Pigulski et al. (2016). An additional decorrelation according to the procedure outlined by Buysschaert et al. (2017) mitigates the impact of the PSF modulation with temperature.

2.2. WIRE

The Wide Field Infrared Explorer (WIRE) was launched on March 4, 1999, but the hydrogen cryogen boiled off soon after launch due to a technical problem, which terminated the primary science mission. The onboard star tracker with 52 mm aperture, however, remained functional and could be used for long-term visual precision photometry until communication with the satellite failed on October 23, 2006 (Buzasi 2002; Bruntt 2007; Bruntt & Southworth 2008). Our target, α Cir, was observed in September 2000, February 2005, and February and July 2006, for a total of 84 days (Bruntt et al. 2009), of which we had access only to the 2005 and 2006 data (16/2/2005 – 1/8/2006).

2.3. SMEI

The Solar Mass Ejection Imager (SMEI) is an instrument on board the Coriolis satellite, which was launched on January 1, 2003. The primary science goal is to detect disturbances in the solar wind, but in doing this, the three CCD cameras observed also the whole sky in successive passes. These data were used to detect, among other things, stellar pulsation (Jackson et al. 2004; Tarrant et al. 2008). α Cir was observed by SMEI from 3rd of February 2003 till 30th of December 2010.

Original SMEI data suffer from very strong instrumental effects. The final light curve was obtained by correcting first for 1-year periodicity, then detrending and sigma clipping, which was repeated up to 25 times. Finally, signals in the vicinity of 1, 2, ... 6 c/d were subtracted. The frequency spectrum of the final data has a sharp decrease at the lowest frequencies, which is the result of detrending. A signal at the satellite orbital frequency, its multiples and side lobes at typically ± 1 and $\pm 2\,d^{-1}$ are also removed. The central wavelength of the SMEI passband is about 630 nm so that the rotation light curve looks similar to BRITE red-filter data. The rotation of α Cir, $f_{\rm rot}$, and $2f_{\rm rot}$, is easily detectable.

2.4. TESS

TESS was launched on April 18, 2018, and has four identical wide-field cameras that together monitor a 24° by 96° strip of the sky and with a red-optical bandpass, covering the wavelength range from about 600 to 1000 nm. Each field is monitored for about 27 days.

The TESS data for α Cir span from April 24 to June 18, 2019, in sectors 11 and 12 with a baseline of 55 days (four 13.7-day orbits). This covers roughly twelve revolutions of α Cir. We downloaded the Simple Aperture Photometry from the MAST portal[1], applied a 3σ outlier clipping, and used the data without any further corrections. As a surface map resolution in longitude of one degree seems to be justified, the 36 124 data points were binned into 4019 time bins, with a maximum bin size of 16.1 minutes. This results in up to nine original data points per bin with a typical scatter of $\pm$ 0.37 mmag. The accuracy of a bin-mean is up to three times better.

[1] https://mast.stsci.edu/portal/Mashup/Clients/Mast/Portal.html

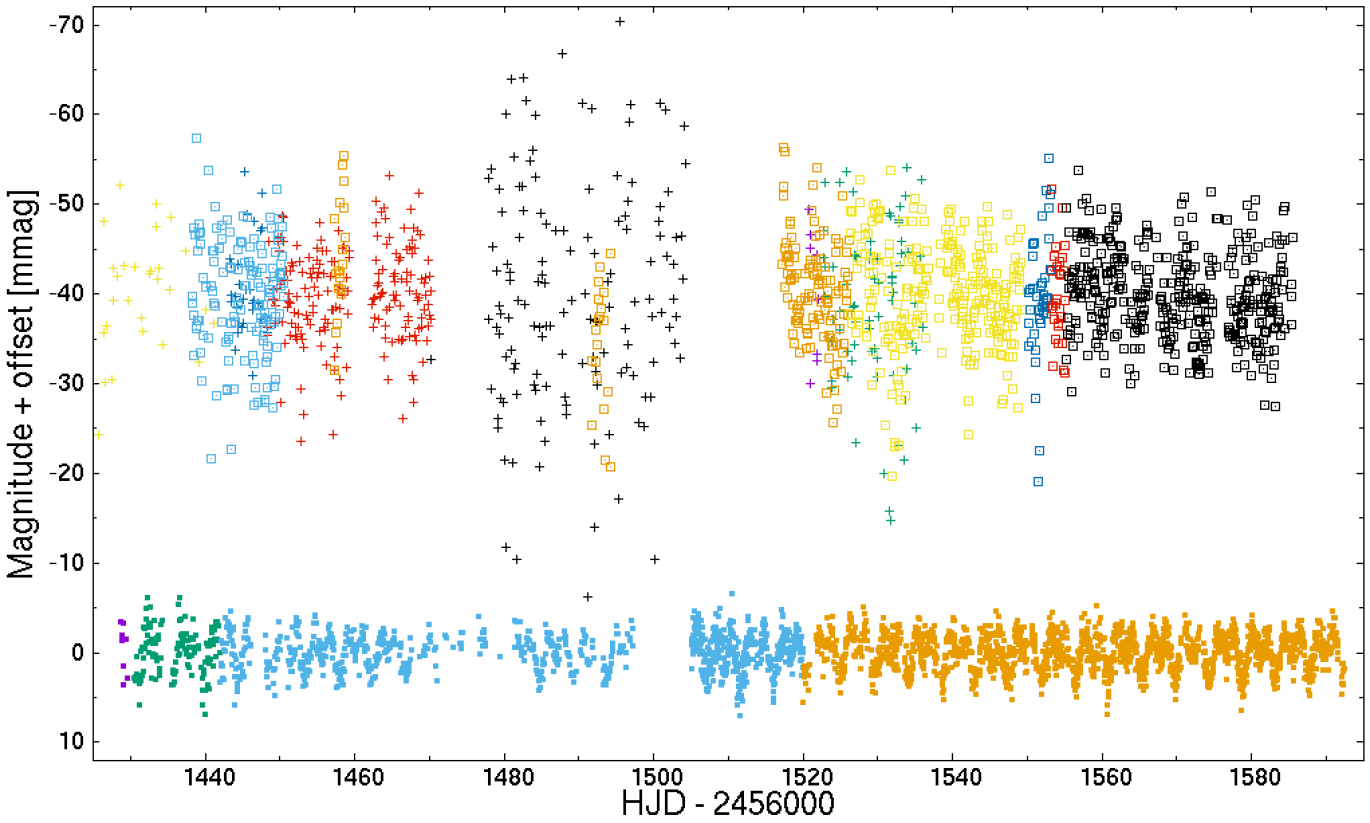

Fig. 1. Decorrelated BRITE photometry with the mean magnitude of respective data sequences subtracted and then averaged over single satellite orbits. Bottom: BTr (small filled squares). Top (vertically shifted for better visibility): BAb (pluses), BLb (open squares). The colours identify different data sequences.

3. Bayesian Photometric Imaging

Our Bayesian photometric imaging technique is described in detail by Lüftinger et al. (2010) and in our Paper I. The number of free parameters, N, depends on the complexity of the stellar surface model considered. The following spot parameters are estimated: longitude, latitude, and area (in practice radius) for each spot, which is assumed to be circular. Therefore, a 3-spot model involves at least 10 free parameters, including the rotation period. In Section 3.3 we comment on the sensitivity of our models to these parameters.

The following parameters were fixed to start with, by already published values:

- Inclination ($i = 36°$). This value results from $v \sin i$ and the stellar radius given by Bruntt et al. (2008).
- Quadratic limb darkening ($U_a = 0.27815, U_b = 0.38195$). As α Cir is a mCP star, limb darkening depends also on rotation phases. Hence, we have to choose a reasonably representative value and base it on a model atmosphere with a $T_{\rm eff} = 7\,500$ K and $\log g = 4.1$ (Kochukhov et al. 2009).
- Contrast between spot and undisturbed photosphere. This has to be fixed because spot area and brightness contrast are highly anti-correlated. The spots are almost certainly bright in the optical wavelengths, as the flux absorbed in the UV is redistributed in the red part of the spectrum for $T_{\rm eff}$ values typical for mCP stars (see Section 4.2. of Paper I). For a start, we assume a contrast of $\kappa = 1.25$ (see also Sec. 3.3.2)

3.1. Bayesian Concept

In a nutshell, a Bayesian approach means the following: An uninformative *prior* probability distribution in the N-dimensional parameter space is converted by the likelihood of the data, given a set of parameter values, into a *posterior* probability distribution. This posterior contains what one can learn from the data in terms of a given model. As it is not possible to visualise a probability distribution of a parameter space of more than three dimensions, it is common practice to extract N marginal distributions, one for each parameter, from the posterior. Each marginal distribution may be summarised by a mean value and, e.g., a 90% credibility interval. In a few cases we use a 68% ('r.m.s.') interval.

In a second step one may determine a model's *evidence* by integrating the posterior probability distribution over the parameter space and dividing by the volume of the latter, because it is the mean probability that matters. This is computationally demanding, but allows one to compare *quantitatively* different models, e. g. a 2-spot model versus a 3-spot model.

The centre of gravity – the barycentre of the N-dimensional posterior 'probability mountain' – is defined by the N parameter mean (expectation) values, computed as described above and it minimises the mean quadratic dispersion. It is this barycentre which makes best use of all the available information as less probable sets of parameter values also contribute to a model's evidence. This 'mean' is more meaningful than the locus of maximum probability, the 'mode' ('best fit'). Only in the rare case of a symmetric probability mountain do 'mean' and 'mode' coincide.

Table 3. Estimated parameter values for our spot models based on BTr, WIRE, SMEI, and TESS photometry. Longitudes are with respect to HJD 2457510.5105 (BRITE), HJD 2453680.6598 (WIRE), HJD 2454115.2887 (SMEI) and HJD 2458625.8020 (TESS), respectively. Spots are ordered according to their impact on the light curve. The set of mean parameter values may differ markedly from the set of modal values due to the skewness of the posterior. Modal values are provided together with mean values and 90% credibility limits. The period is given in days and the residuals are r.m.s. values.

	BTr		WIRE		SMEI		TESS	
	mean	mode	mean	mode	mean	mode	mean	mode
spot#1:								
longitude (°)	0^{+4}_{-4}	9	0^{+2}_{-2}	0	0^{+7}_{-7}	358	$0.0^{+0.3}_{-0.3}$	0.0
latidtude (°)	-27^{+14}_{-17}	-63	37^{+5}_{-5}	43	-19^{+16}_{-28}	-10	$-2.7^{+0.6}_{-0.5}$	-2.4
radius (°)	21^{+12}_{-9}	52	14^{+3}_{-3}	17	19^{+20}_{-9}	14	$9.7^{+0.1}_{-0.1}$	9.7
spot#2:								
longitude (°)	171^{+4}_{-5}	183	179^{+3}_{-4}	178	155^{+7}_{-7}	155	$144.4^{+0.5}_{-0.5}$	144.5
latidtude (°)	-30^{+12}_{-12}	-37	40^{+6}_{-6}	44	46^{+25}_{-23}	67	$20.7^{+0.6}_{-0.6}$	20.9
radius (°)	21^{+9}_{-8}	24	13^{+3}_{-3}	17	8^{+2}_{-2}	10	$6.7^{+0.1}_{-0.1}$	6.7
spot#3:								
longitude (°)	111^{+20}_{-20}	133	120^{+2}_{-2}	120	–	–	$171.9^{+0.6}_{-0.6}$	171.7
latidtude (°)	34^{+29}_{-22}	-4	-10^{+2}_{-2}	-11	–	–	$-36.1^{+5.3}_{-5.1}$	-36.8
radius (°)	6^{+1}_{-1}	9	9^{+1}_{-1}	9	–	–	$16.9^{+4.2}_{-4.3}$	17.5
period (days)	4.4779 ±0.0012	4.4781	4.47925 ±0.00009	4.47926	4.47912 ±0.00018	4.47912	4.4803 ±0.0004	4.4803
residuals (mmag)	±1.386		±0.318		±6.232		±0.141	

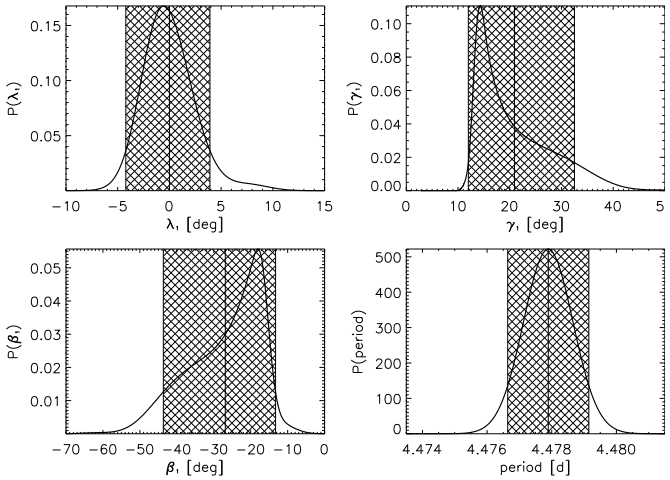

Fig. 2. Left: spot #1 marginal distributions of longitude (λ) and latitude (β) in degrees. Right: spot radius (γ) and period in days. The vertical lines indicate the mean value and the 90% credibility limits (shaded area). All deduced from BTr data. Because of the skewness of the distribution the locus of maximal probability does not necessarily coincide with a parameter's mean value.

A corresponding picture could be: compare the height of Matterhorn in Switzerland with that of Cape Town's Table-Mountain in South Africa and quote their positions. The case of Matterhorn is trivial. It has a nice, nearly symmetric structure and an obvious peak above the timberline, but Table Mountain raises a problem. Is the position of the mini-peak at the border of the Table (location of the 'mode') to be listed, or is it more appropriate to quote the geographical centre (centroid, 'mean') of the plateau?

Probabilistic methods are not primarily aiming for a single 'best-fit' solution of a given problem but for the posterior distribution of the various model parameters and how well a model reproduces the observations *compared to other models*. However, for the sake of completeness, we also provide modal values in Table 3.

As an illustration we present Fig. 2 concerning our preferred 3-spot model deduced from the BTr data. It shows the marginal distributions for longitude, latitude, and radius of the first spot (#1) – which has the largest impact on the light curve –, and the marginal distribution for the rotational period. Each marginal distribution results from integrating the N dimensional posterior over the corresponding $(N-1)$ dimensional sub space. The boundaries of the 90% credibility interval as well as the parameter mean are indicated by vertical lines. The widths and asymmetries of the marginal distribution for latitude and radius indicate that these two model parameters are poorly defined, whereas spot longitude and rotation period are much better constrained by the data.

It should be noted that finding the posterior's mode is computationally fast in comparison to the Markov-Chain Monte-Carlo (MCMC) integrations, which are necessary to provide mean values and credibility intervals.

More about spots will be discussed in Sec. 3.3.

3.2. Rotation

An early estimate for a rotation period, based on magnetic field measurements (Wood & Campusano 1975) and H_α polarime-

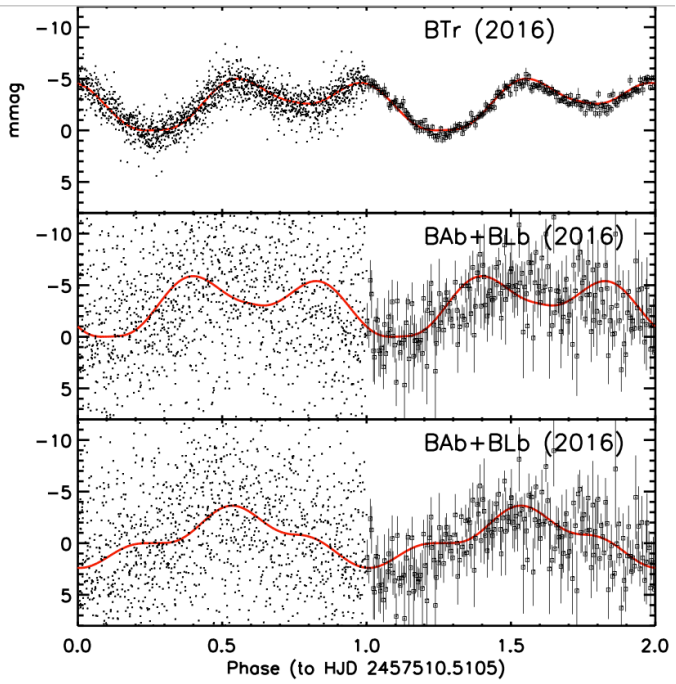

Fig. 3. Rotation modulation of α Cir photometry with $P_{\rm rot}$ = 4.4779 d. For the phase interval from 0 to 1.0 orbit mean values are shown, and for the phase interval from 1.0 to 2.0 data binned into 200 phase bins. Top: 3-spot model derived from the 'red' BTr data. Middle: Fit of the 'red' 3-spot model from the top to the 'blue' BAb+BLb data, which requires a phase shift of 0.16 ± 0.02, and a reduction of the spot-surface brightness. Bottom: Same 3-spot model, but with spots of different brightness contrast, and with spot #1 appearing even darker in the 'blue'. A slightly different zero-point was used for binning the bottom light curve data.

try (Landstreet 1980), is given in Mathys (1991) who speculates that the star has a magnetic field varying with a period of more than two weeks. The next estimate was published by Kurtz et al. (1993) with $P_{\rm rot} = 0.99535$ d, based on the modulation of the star's main pulsation frequency obtained during a 99 h high-speed photometric observing run in 1992. Multi-site observations in 1993, however, indicated a rotationally modulated amplitude of the main pulsation frequency of α Cir, suggesting a $P_{\rm rot} = 4.463 \pm 0.010$ d (Kurtz et al. 1994). The authors also reanalysed Johnson B data spanning the years 1981 to 1993 and refined the rotation period to $P_{\rm rot} = 4.4790 \pm 0.0001$ d. Later, Balona & Laney (2003) analysed 548 high-dispersion spectra obtained during five nights of a seven night observing run in 2002 and conclude a $P_{\rm rot}$ of 4.463 d.

Based on sparse magnetic field data spanning 14 years, Bychkov et al. (2005) determined $P_{\rm rot} = 4.4794$ d which is only marginally different from what Bruntt et al. (2009) derived from WIRE data ($P_{\rm rot} = 4.4792 \pm 0.0004$ d). The authors also extended the investigation of Bychkov (op.cit.) by including new data from Hubrig et al. (2004) and '... find a marginal indication of magnetic variability with the known rotation period $P_{\rm rot} = 4.4794$ d, at the 2.5σ significance level, if one outlying positive field measurement is ignored'.

The stellar rotation period is observationally the most obvious parameter and can be estimated, in principle, without any model. However, here we consider the rotation period as an unknown parameter of a 3-spot model. From the averaged BTr data (2016) alone one gets a rotation period of 4.4779 ± 0.0012 d (cf. Tab. 3 and Fig. 3, top and middle panels). A period of 4.4779 d coincides with the 'standard' value of $P_{\rm rot} = 4.4790$ d within 1.4σ.

A re-analysis of the red BRITE 2014 data from Paper I, with the rotation period being a further free parameter in our Bayesian analysis, indicate a $P_{\rm rot} = 4.4846 \pm 0.0017$ d (68% interval), which exceeds the 'standard' value of 4.4790 d by 0.12%, or 3.3 σ. A similar analysis of the WIRE data indicates a rotation period of $P_{\rm rot} = 4.47925 \pm 0.00009$ d. Our analysis of SMEI data in terms of two bright spots results in $P_{\rm rot} = 4.47912 \pm 0.00018$ d (see Tab. 3).

A comparison of spot #1 transit times from WIRE and TESS (3-spot model), respectively, resulted formally in $P_{\rm rot} = 4.47930 \pm 0.00002$ d (68% interval), assuming that there are 1104 stellar revolutions between the corresponding maps in Fig. 4.

3.3. Spots

A major challenge is estimating the number of spots necessary to get a good fit without over-fitting. In Paper I we were able to identify one bright spot in the BRITE-blue data, two spots in BRITE-red and WIRE data, but there were already hints for a more complex surface map, at least in the 'red' case. Not surprisingly, the photometric quality of the data matters. In contrast to the 2014 data, the 2016 BRITE-Toronto (BTr) data convincingly indicate a 3-spot model. The reduction in credibility, which is a formal consequence of an increased number of free parameters from 7 (two spots) to 10 (three spots) is more than compensated by an improved goodness-of-fit value. To our knowledge, this is the first time that the evidence of models differing in the number of spots has been probabilistically determined.

Let us recall Section 3.1: Integration of the posterior probability density over the parameter space and dividing by the volume of the latter provides the evidence of a model. Roughly speaking, the model evidence is kind of a *mean* weighted likelihood and its value depends on the volume of parameter space considered.

With the Markov-Chain Monte-Carlo (MCMC) technique and the availability of PC clusters, an integration over a high-dimensional configuration space is meanwhile computationally feasible. With computed evidence one is able to compare quantitatively the performances of models differing in the number of spots by considering the evidence ratio, i.e. the Bayes factor.

3.3.1. Red maps

For the red data obtained with BTr, the credibility gain from a 2-spot model to a 3-spot model, expressed by the ratio of the evidence, is approximately $1.2 \cdot 10^6$. This large Bayes factor is due to the big number of data points (1678) involved. The residuals to the photometry decreased slightly from 1.389 to 1.386 mmag and the mean credibility gain *per data point* is 0.8 per cent ($(1.2 \cdot 10^6)^{1/1678} = 1.008$) in favour of the 3-spot model. Table 3 summarises our 3-spot model MCMC calculations based on BTr, WIRE, SMEI, and TESS photometry. The resulting maps are illustrated in Fig. 4. The tenth parameter listed in Table 3 is the rotation period with 90% credibility ranges. Be aware that the usual 68% interval for $P_{\rm rot}$ is of course smaller by a factor of 1.645, e.g. for BTr: ± 0.0008 d.

The BTr maps are based on 62735 BTr input data points obtained in 2016, and binned in 1678 time bins according to individual BRITE orbits. A graphic presentation can be found in Fig. 4, left column.

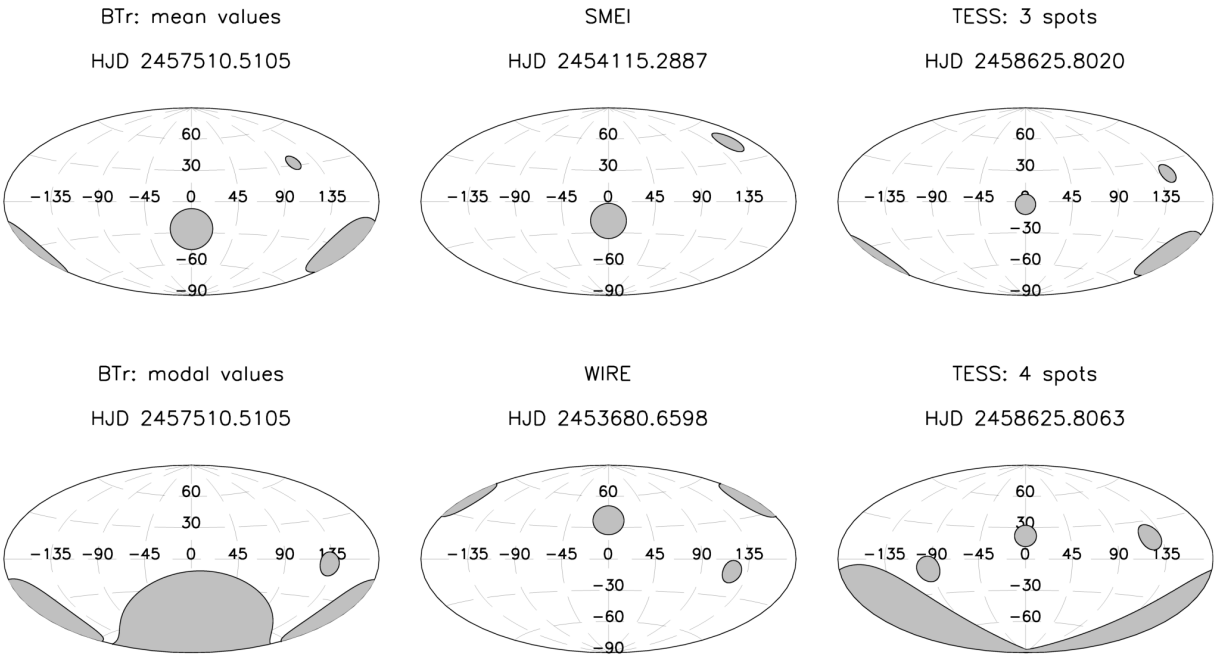

Fig. 4. HJDs are transit times of the spot which contributes most to the light curve (spot #1). Left: BTr based maps (top: mean values; bottom: modal values). Middle: SMEI mean map which allows only for two spots (top) and WIRE (bottom), which prefers a three spot map. Right: Comparison of TESS mean maps allowing for three spots (top) and for 4 spots (bottom), respectively.

The rather poor photometric quality of the SMEI data does not allow one to obtain a 3-spot model, because the MCMC algorithm simply does not converge; only two spots can be identified (Fig. 4, top in middle column).

The surface map based on nearly 55 days of TESS (2019) photometry (Fig. 4, right column), confirms basically the map derived from BTr (2016) data. Overall, the TESS data quality is impressive and encourages one to look for a fourth spot (cf. Table 4, and Fig. 4). The addition of another spot is rewarded by a substantial gain in goodness-of-fit. The residuals drop from ±0.141 mmag (3-spot model) to ±0.125 mmag. A period as low as 4.4779 days seems to be excluded by the more accurate TESS photometry.

A comparison of, e.g., the maps on top (SMEI) and at the bottom (WIRE) of Fig. 4, middle column, seems to imply that the orientation of a map is flipped relative to the equator. This illustrates the difficulties one encounters when trying to convert a one-dimensional light curve into a two-dimensional surface map. While period and spot longitudes are comparatively well defined, estimating spot latitudes notoriously proves ill-posed unless the S/N is very high. Fig. 5 illustrates the problem, showing two alternative WIRE maps which are only marginally inferior to the solution shown in Fig. 4, but with spot latitudes comparable to maps from BRITE and TESS data.

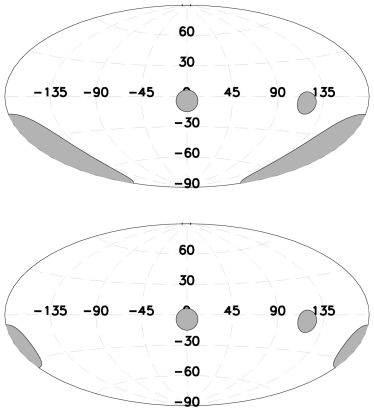

Fig. 5. Example of two maps derived from the same WIRE data. Both maps fit the light curve with an r.m.s. error only 0.002 mmag larger than the WIRE map presented in Fig. 4.

3.3.2. Blue maps

In a next step we reanalysed the much noisier blue data obtained with BAb and BLb.

A reduced data quality impacts, of course, the sophistication of testable models (i.e. the number of free parameters). These are limited as much as possible by fixing all but one parameter, the brightness contrast κ, when applying our 3-spot model, derived from the BTr data with ten free parameters (Table 3), to BAb and BLb data. We recall that up to now, i. e. for the red case, we assumed $\kappa = 1.25$ which controlled also the spot size. When applying our red model to the blue data, but allowing the contrast κ to be a free parameter, we found a contrast $\kappa = 1.05 \pm 0.04$, albeit with residuals as large as ±5.9 mmag (r.m.s.). Recall that the blue photometry is about a factor of four noisier than the red photometry (see Figs. 1 and 3, and Paper I). If one allows for a time lag, Δt, in the model, the fit improves: $\kappa = 1.23 \pm 0.035$, and $\Delta t = 0.69 \pm 0.08$ d, with residuals of ± 5.1 mmag (r.m.s.). The time lag of ≈ 17 hours is equivalent to a phase shift of 56° ± 7°.

When further increasing the parameter space by assigning each spot an individual surface brightness (bright/dark: κ is larger/smaller than 1), one can avoid a phase shift. In the latter case the 'blue' spot #1 completely disappears and, hence, the solution converges to a 2-spot model with a Bayesian evidence comparable to the 3-spot solution requiring a phase shift.

Table 4. Parameter values for our 4-spot model based on binned TESS (2019) data (4019 points). Spots are ordered according to their impact on the light curve. In addition to mean values the 90% credibility limits are given along with the modal ('best fit') values. Spot longitudes are with respect to HJD 2458625.8063 (transit time of spot # 1, see also Fig. 4, bottom of right column), and the residuals are r.m.s. errors.

	TESS	
	mean	mode
spot#1: longitude (°)	$0.0^{+1.0}_{-1.0}$	-0.2
latitude (°)	$22.1^{+1.1}_{-1.1}$	22.2
radius (°)	$10.3^{+0.8}_{-0.9}$	10.5
spot#2: longitude (°)	$124.0^{+1.7}_{-1.6}$	123.8
latitude (°)	$17.2^{+3.4}_{-3.5}$	18.2
radius (°)	$10.1^{+0.5}_{-0.5}$	10.2
spot#3: longitude (°)	$198.8^{+1.4}_{-1.5}$	199.3
latitude (°)	$-48.8^{+3.3}_{-3.4}$	-48.0
radius (°)	$45.0^{+1.7}_{-1.7}$	44.6
spot#4: longitude (°)	$265.9^{+0.9}_{-0.9}$	266.0
latitude (°)	$-8.6^{+0.8}_{-0.8}$	-8.4
radius (°)	$11.0^{+1.7}_{-1.8}$	11.5
period (days)	$4.4799^{+0.0003}_{-0.0003}$	4.4799
residuals (mmag)	±0.125	

Dropping the restriction for bright ($\kappa > 1$) spots only, one would get an even better fit (see Fig. 3) for the blue data (±5.0 mmag (r.m.s.)) with a dark ($\kappa_1 \simeq 0.84$) spot #1. In Paper I it is argued why spots are expected to be bright.

In conclusion, the presently available blue photometry is insufficient for a reliable and convincing photometric surface mapping.

4. Pulsation of α Cir

In the following we use the same numbering of frequencies as was used by Bruntt et al. (2009) and in Paper I.

No pulsation is detected in the SMEI data with an amplitude exceeding 0.33 mmag, which corresponds to a S/N of 4.5. This is somewhat surprising, given that the amplitude of the dominant pulsation frequency, f_1, in the combined 2014 and 2016 BRITE-red data, with a similar effective wavelength, is equal to 0.57 mmag (see Fig. 6 and later in this section). The amplitude in the WIRE data is equal to 0.65 mmag. However, the SMEI passband is very wide and corresponds to the sensitivity curve of a front-illuminated CCD, which ranges between 400 and 1000 nm (see Tab. 1). Given different shapes, amplitudes, and phases of the rotational modulation of α Cir at different wavelengths, it might well be that the pulsation signal has a too small amplitude in "white-light" SMEI data. Inappropriate averaging could be another explanation. Unfortunately, we do not know all the details of the SMEI photometry. A single SMEI data point comes from a series of 4-s exposures, where it is not always clear how many individual exposures are combined. This depends on the time a star passes through the camera field of view ($3° \times 60°$), and changes with the aspect angle. Thus, the minimum total time is slightly less than one minute, but can also be longer.

Table 5. Detected frequencies in the various time series of α Cir, where BRr and BRb are the combined 2014 and 2016 data sets of the red (BTr) and blue (BAb and BLb) BRITE observations, respectively. Phases are defined for HJD = 2457200 and are given in degrees. The parameter p gives the probability if a frequency is statistically significant compared to no signal (i.e. due to noise).

	Frequency $[d^{-1}]$	Amplitude [parts per thousand]	Phase degrees	p
		f_1		
TESS	210.99512(15)	0.394(8)	-	1.0
WIRE	210.99361(5)	0.65(1)	-	1.0
BRr	210.99329(2)	0.577(28)	95(1)	1.0
BRb	210.99327(2)	1.716(81)	84(1)	1.0
		$f_{1-} = f_1 - f_{\rm rot}$		
TESS	210.7716(6)	0.049(3)	-	1.0
WIRE	210.7702(1)	0.083(4)	-	1.0
BRb	210.7866(2)	0.263(86)	-	0.31
		$f_{1+} = f_1 + f_{\rm rot}$		
TESS	211.2188(7)	0.039(3)	-	1.0
WIRE	211.2171(1)	0.074(4)	-	1.0
BRb	211.2167(1)	0.334(86)	-	0.82
		f_6		
TESS	208.3879(3)	0.089(3)	-	1.0
WIRE	208.3866(1)	0.145(4)	-	1.0
BRr	208.3888(1)	0.098(30)	23(7)	0.77
BRb	208.3890(1)	0.318(82)	11(5)	0.91
		f_7		
TESS	213.6055(3)	0.105(3)	-	1.0
WIRE	213.6004(1)	0.186(4)	-	1.0
BRr	213.6005(1)	0.195(29)	92(4)	0.99
BRb	213.6011(2)	0.375(83)	76(7)	0.99

We also cannot exclude a variable pulsation signal, either intrinsic or apparent, e.g. due to the presence of a companion. This would reduce the pulsation amplitude in the frequency spectrum, if the variability time scale is shorter than the time span of SMEI observations (about 7.9 years). Unfortunately, the noise is too large to verify this hypothesis.

After subtracting the rotational modulation from the (unbinned) original TESS time series, the Fourier amplitude spectrum shows a rich pattern of pulsation modes in the vicinity of f_1. However, a detailed analysis of this is beyond the scope of the present paper and we instead refer to a follow-up study that will present a detailed asteroseismic analysis (Kallinger et al, in preparation). Here, we use the oscillations in the TESS data primarily to guide and verify the analysis of the BRITE observations. For comparison we also show in Fig. 6 and 7 the Fourier

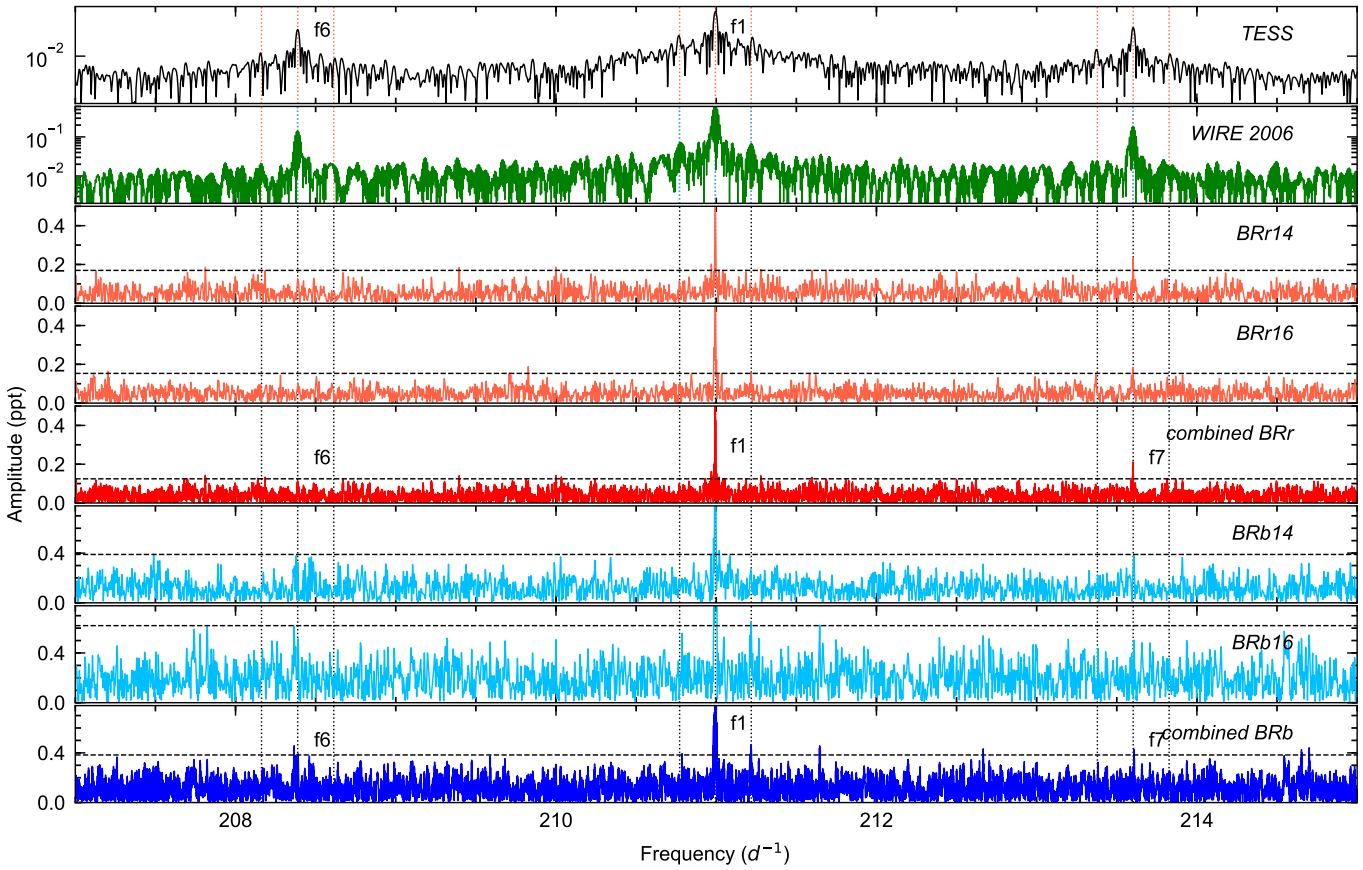

Fig. 6. Fourier amplitude spectra from different sources around the primary pulsation period of α Cir. BRr14, BRr16, BRb14, and BRb16 are the red and blue BRITE data, obtained during the years 2014 and 2016, respectively. Vertical dotted lines indicate the oscillation modes and the rotational sidelobes identified in the TESS data. Horizontal dashed lines mark a S/N = 3.

spectrum of the combined 2006 WIRE data (~170 d with a 114 d gap in between).

4.1. Primary pulsation frequency f_1

After subtracting the rotational modulation via spline fits in the rotation phase domain, the primary pulsation frequency (f_1) at about 210.99 d^{-1} is easily detected in all four BRITE datasets (Fig. 6), which we briefly call BRb14 (all blue filter data from the year 2014), BRb16 (2016), BRr14 (all red filter data, 2014), and BRr16 (2016), respectively. Combining the 2014 and 2016 data results in a total time base of ~840 d with a coverage of about 35%. Merging the data improves the frequency resolution as well as the S/N (Fig. 6) but, as can be seen in Fig. 7, the ~540 d long gap between the two data sets causes strong aliasing with about $\pm 0.0019 d^{-1}$ and multiples. Fig. 7 also indicates that the amplitudes in the 2016 data seem to be slightly higher than in the 2014 data. Hence, an even smaller amplitude for SMEI, some years earlier, is not surprising.

To extract the oscillation parameters from the various light curves, we use a probabilistic approach presented by Kallinger & Weiss (2017). The automated Bayesian algorithm was originally developed to deal with multiple frequencies within the formal frequency resolution (Kallinger et al. 2017) but works with a "mono-periodic" signal (within one formal frequency resolution bin) as well. The method uses the nested sampling algorithm MultiNest (Feroz et al. 2009) to search for periodic signals in time series data and tests their statistical significance (i.e. to be not due to noise) by comparison with a constant signal. A solution is considered real[2] if its probability $p = z_{\rm signal}/(z_{\rm signal} + z_{\rm noise}) > 0.9$, where z is the global evidence[3] delivered by MultiNest.

Fig. 7 shows highly significant peaks at about $210.9933 d^{-1}$ in the combined BRr and BRb data, which compare visually well to those found in the WIRE and TESS data. The best-fit solutions are listed in Tab. 5. The uncertainties might appear unrealistically small, especially for the TESS data with a time base of less than 1/15 of the combined BRITE data. However, the frequency uncertainty is also influenced by the S/N of a frequency (e.g. Kallinger et al. 2008), which is significantly larger in the TESS data than in the BRITE data (S/N $\simeq$ 14).

While the frequencies extracted from the red and blue BRITE data agree exceptionally well with each other (within $0.00002 d^{-1}$ or 30 μs at a period of 409.4917 s), there are small but significant differences to the frequencies found in the WIRE ($0.0003 d^{-1}$) and TESS ($0.0018 d^{-1}$) data. Such offsets might indicate a variable f_1 due to, e.g., a companion or evolutionary effects, but also aliasing in the BRITE data could (at least partly) explain this. Even though the strongest peak in the BRr and BRb data is nearly identical (see Fig. 7), it might be that the actual

[2] According to the convention established by Jeffreys (1961), the evidence for or against one of two hypotheses is considered "substantial" for $p \gtrsim 0.75$, "strong" for $p \gtrsim 0.91$, and "very strong" for $p \gtrsim 0.97$.

[3] The global evidence is a normalised logarithmic probability describing how good the model fits the data with respect to the uncertainties, parameter ranges, and the complexity of the fitted model.

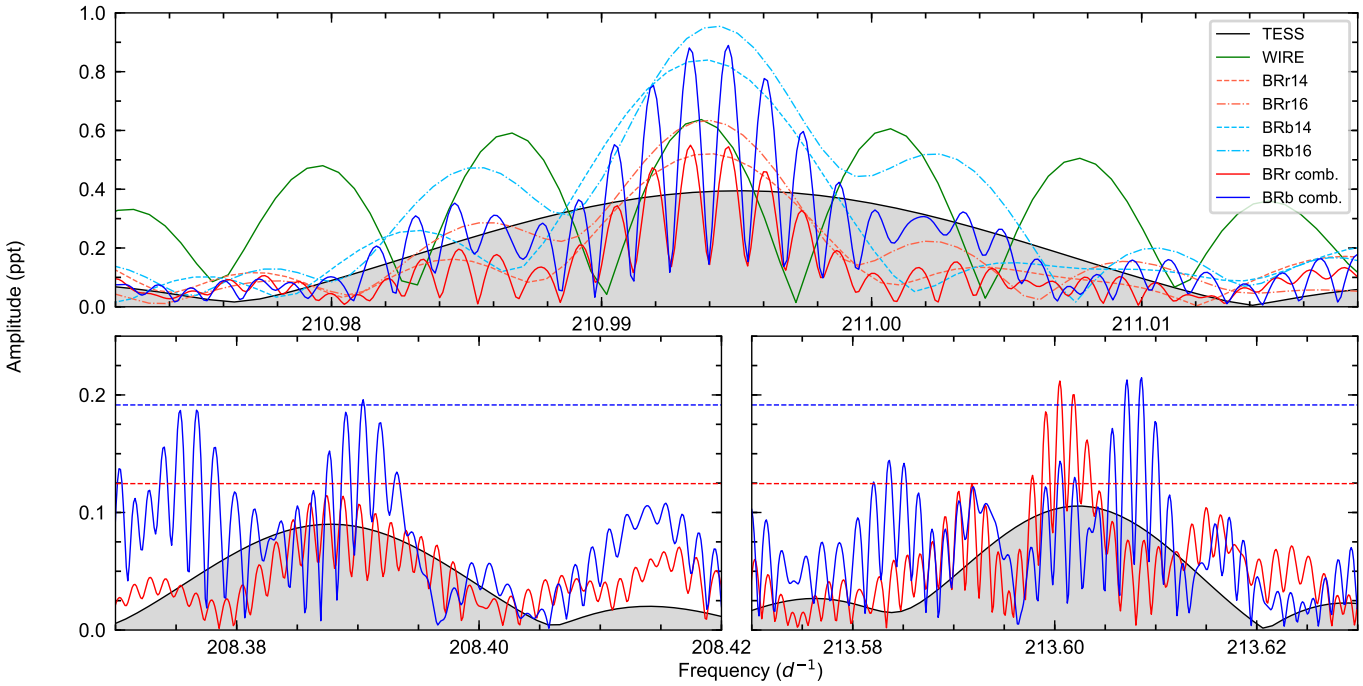

Fig. 7. Fourier amplitude spectra of the TESS and BRITE photometry centred on f_1 (top), f_6 (bottom left), and f_7 (bottom right). The blue BRITE amplitude spectra are divided by two for better comparison with the other data. Dashed lines indicate a S/N of three.

peak is one of the neighbouring alias peaks. If we consider the alias at $+0.0019 d^{-1}$ as the true frequency then it would almost perfectly resemble the TESS result. However, forcing our frequency analysis algorithm to fit this peak and comparing the resulting global evidence to the original one gives a probability of 0.97 against this scenario.

In Table 5 we also provide the phase of f_1 in the blue and red filter, and determine a phase difference of $11° \pm 2$, which is consistent with the phase lags between Johnson B and V of $7.4° \pm 5.1$ derived by Kurtz et al. (1993) and the value given in Paper I ($10.6° \pm 5.9$). Unfortunately, we cannot compare this to phases in the WIRE and TESS data. The slightly different frequencies we find in the data cause accumulated phase shifts (relative to the time of the BRITE observations) of more than 2.6 and 1.1 oscillation cycles for TESS and WIRE, respectively, so that comparing any phases becomes meaningless.

In conclusion, the average value for f_1, based on *all* BRITE data (years and colours) is $210.99328(2)\,d^{-1}$. In addition, we find evidence that this frequency changes over time, but we leave a more detailed discussion to a follow-up study.

With the new BRITE data, we have computed Fig. 8, which is an analog to Fig. 11 in Paper I, that is the change of amplitude and phase of f_1 with the rotation phase. The values for the phases given in this new figure differ from those in the figure of Paper I, because different rotation periods have been used. The data are binned into ten rotation phases where the starting epoch and the rotation period are the same for phasing the rotational changes.

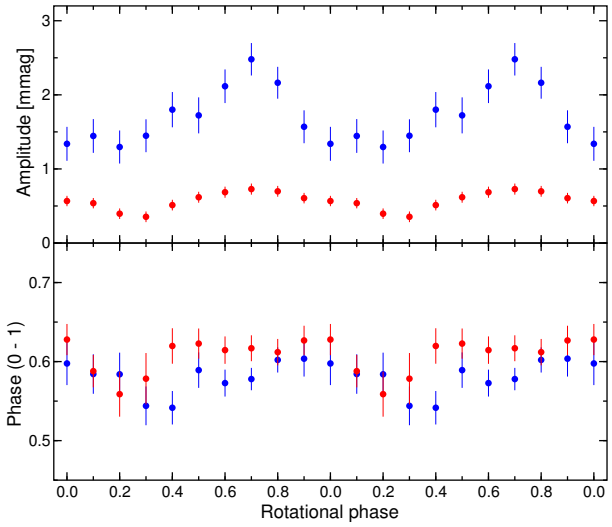

Fig. 8. Change of amplitude and phase of f_1 with the rotation phase for the blue BRITE data (blue dots) and red data (red dots), respectively, computed for the combined 2014 and 2016 data set.

4.2. Additional pulsation frequencies (f_6, f_7, and rotational side lobes of f_1)

After prewhitening f_1 from the combined BRITE data we still find some signal left at frequencies where Bruntt et al. (2009) reported f_6 and f_7 in the WIRE data and which are unambiguously confirmed by TESS (see Fig. 6). Even though the corresponding peaks barely exceed a S/N of three in the individual 2014 and 2016 BRITE data, they reach sufficient significance levels in the combined data (Tab. 5). Given the larger amplitude, f_7 reaches a probability of 0.99 (and therefore very strong evidence to be not due to noise) in both data sets. On the other hand, f_6 has a smaller amplitude and therefore also a lower probability of 0.91 (strong evidence) in the BRb data and 0.77 (still substantial evidence) in the BRr data. Note that we would not consider the latter peak as real on its own, but given its significance beyond doubt in all other time series we take it for real in the BRr data. In a more Bayesian sense, one could, e.g., use the TESS frequency (and its uncertainty) as a prior in the frequency analysis of the

BRr data, but such an approach would exceed considerably our computational resources. This would significantly increase the peak's probability to be not due to noise.

Even though f_6 and f_7 are well detectable in the combined BRITE data, we find again an aliasing problem when determining their best-fit parameters. A closer look at Fig. 7 shows that while the strongest peak in the BRr spectrum is consistent with the position of f_7 in the TESS data, the dominant peak in the BRb spectrum is shifted towards higher frequencies. However, the BRb16 time series has several large gaps with the longest being about 12.9 d long, which causes aliases at about $\pm 0.078\,\mathrm{d}^{-1}$ (on top of the $\pm 0.0019\,\mathrm{d}^{-1}$ aliases due to the large gap between the 2014 and 2016 data). If we now force our frequency analysis algorithm to fit the alias at $-0.078\,\mathrm{d}^{-1}$ instead of the largest-amplitude peak, we get very good agreement between BRr and BRb data. Such a strategy might appear arbitrary but in fact represents the Bayesian principle of a prior information and is therefore justified.

We find a similar situation for f_6. While the largest-amplitude peak in the BRr spectrum agrees well with the position of the peak in the TESS data, the dominant peak in the BRb spectrum appears to be a $+0.0019\,\mathrm{d}^{-1}$ alias. A forced fit again aligns the frequencies we find in the blue and red BRITE data.

Finally, we find also some signal in the BRb data at the expected rotational side lobes of f_1. The pulsation amplitude of an obliquely pulsating non-radial mode changes with the rotation phase, as the aspect of the mode changes. This gives rise to frequency side lobes $f_1 \pm f_{\mathrm{rot}}$, that describe the amplitude modulation (and phase variation, if present), which are clearly visible in the WIRE and TESS data. While the signal at f_{1-} is too weak to be distinguished from the noise (we even know it has to be there), the peak at f_{1+} is with $p = 0.82$ statistically significant. This allows for a seismic determination of α Cir's rotation period, which is with 4.4758 ± 0.0020 d more accurate than those resulting from the WIRE and TESS data. Despite the larger noise of BRITE data, the much longer time base allows for a more accurate determination of P_{rot}.

4.3. Mode identification and the large frequency separation

A frequently used observable in asteroseismic studies of high-overtone acoustic oscillations is the large frequency separation $\Delta\nu_{n,l}$, which is defined as the difference between modes of the same spherical degree and consecutive radial orders, $\nu_{n+1,l} - \nu_{n,l}$. The large separation becomes relevant for high radial orders, which are expected to follow the asymptotic relations (Tassoul 1980):

$$\nu_{n,l} \simeq \Delta\nu_{n,l}\,(n + l/2 + \epsilon_0) - l(l+1)D_0, \qquad (1)$$

where ϵ_0 and D_0 are parameters sensitive to the properties of the reflection layer near the stellar surface and the conditions in the stellar core, respectively. But more important, the large separation is related to the stellar acoustic diameter (i.e. inverse sound travel time across the stellar diameter). For an ideal adiabatic gas, this is proportional to the square root of the mean stellar density. Consequently, $\Delta\nu$ provides a measure for the mean density of a star.

Even though the presence of a strong magnetic field might distort spherical symmetry, the high-frequency oscillations observed in α Cir indicate that these modes are high-overtone acoustic oscillations for which one may expect to find a regular pattern corresponding to the asymptotic relation. As already noted by Bruntt et al. (2009), the three modes f_1, f_6, and f_7 are almost equidistant in frequency with an average separation of $\sim 2.606\mathrm{d}^{-1}$. One can naively expect that this value corresponds to the average frequency separation of α Cir. However, it is not compatible with other constraints of the star as we show in the following.

Bruntt et al. (2008) determined the angular diameter of α Cir to $\Theta_{LD} = 1.105 \pm 0.037$ mas, and used the revised Hipparcos parallax of van Leeuwen (2007) to estimate the star's radius to be $1.97 \pm 0.07\,\mathrm{R}_\odot$. With an average frequency separation of $\sim 2.606\mathrm{d}^{-1}$ one can estimate the star's mass according to $\Delta\nu \propto \sqrt{M/R^3}$. This is usually done by relating $\Delta\nu$ to the solar value of about $11.664\,\mathrm{d}^{-1}$ (e.g. Kallinger et al. 2010), which gives an unrealistically small mass of $0.38 \pm 0.04\,\mathrm{M}_\odot$. However, if we follow Bruntt et al. (2009) and set $\Delta\nu = 5.21\,\mathrm{d}^{-1}$ (i.e., f_7 - f_6), we obtain a plausible mass of $1.52 \pm 0.15\,\mathrm{M}_\odot$, that is also compatible with the estimate of $1.7 \pm 0.2\,\mathrm{M}_\odot$, based on the star's position in the HR-diagram (Bruntt et al. 2008). In fact, we expect α Cir to be slightly more massive than $1.5\,\mathrm{M}_\odot$ because the observed modes are magnetically distorted so that the distortion increases with decreasing frequency (e.g. Cunha 2006). The large separation of the unperturbed modes is therefore larger than that observed, which makes the star more massive than one would expect from its observed $\Delta\nu$.

A consequence of $\Delta\nu$ being more likely equal to $5.21\,\mathrm{d}^{-1}$ than to $2.606\,\mathrm{d}^{-1}$ is that the three modes discussed above cannot be of the same spherical degree. This is also supported by Fig. 9, where we show the three modes in an Echelle diagram. The modes almost perfectly line up vertically when folding their frequency with $2.6\,\mathrm{d}^{-1}$ (indicating the same spherical degree). Not so if folding them with $5.2\,\mathrm{d}^{-1}$. Then f_1 is shifted by slightly more than one half in horizontal direction while the other two modes have about the same horizontal offset. This is in fact expected for a sequence of two consecutive $l = 0$ modes with an intermediate $l = 1$ mode, or vice versa (see Eq. 1). Since Bruntt et al. (2009) argued that f_1 is very likely an axisymmetric dipole mode ($l = 1, m = 0$) based on simulated amplitude modulations for an oblique pulsator model, we conclude that f_6 and f_7 are most likely consecutive radial modes.

Further support for this is provided by the amplitude ratios and phase differences in the two BRITE pass bands we determine for the three modes (Fig. 9). One can expect that modes of the same spherical degree form clusters in a diagram like Fig. 9. If one finds modes that are clearly separated in the amplitude-ratio versus phase-difference plane, they can be assumed to have different spherical degrees. For f_6 the uncertainties are too large to make any conclusions, but f_1 and f_7 are separated by about $1.8\,\sigma$ in their amplitude ratio, which corresponds to a probability of almost 0.9 to be separated and therefore to have a different spherical degree.

5. Discussion

– Data: We analyse and discuss data obtained by BRITE-Constellation during 2014 and 2016, covering a total of 316 days. In addition, data extracted from various archives obtained with WIRE in 2005 and 2006, and by SMEI, which observed α Cir for nearly nine years, and with TESS extend considerably the available data volume and time base.

Clearly, these data suffer from different noise levels and instrumental effects, which need to be considered and corrected. Corrections of trends and averaging procedures need to be optimised for a discussion of long-term (rotation, spots) and short-term (pulsation) effects, respectively. An attractive aspect of the

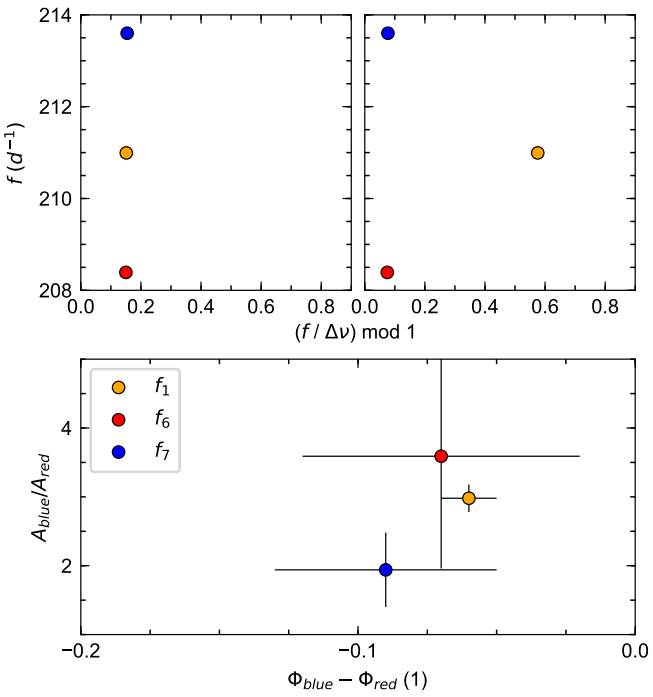

Fig. 9. *Top*: Echelle diagrams including the three frequencies detected in the BRITE data with a large separation $\Delta\nu = 2.6\mathrm{d}^{-1}$(left), and $5.2\mathrm{d}^{-1}$(right). *Bottom*: Amplitude ratios vs. phase differences in the two BRITE bands for the same frequencies.

BRITE data is the availability of data in two passbands, some of them taken nearly simultaneously. This allowed us to study in detail pros and cons of Bayesian based photometric surface imaging.

Not surprisingly, the photometric quality of the data seriously limits the number of detectable spots and their location, as is discussed in Section 3.3. Whereas spot longitudes are well constrained by the data, latitudes are, photometrically, a notoriously ill-defined parameter. In the case of Doppler imaging, the situation is much better due to the availability of additional information.

– Rotation: The determination of $P_{\rm rot}$ for α Cir dates back to 1991 (Mathys 1991). Meanwhile, many photometric, spectroscopic and polarimetric observation were performed and we determined the formally most accurate $P_{\rm rot}$ from combinded WIRE and TESS spot transit times to be 4.47930 ±0.00002 d (68% interval), However, this value differs significantly from that derived from TESS data alone.

The different shape of the rotation phase-plot extracted from the red and blue data indicates a different chemical composition of one of the spots, which, however, can only be tested by high resolution spectroscopy.

– Spots: Two spots were identified in Paper I in the red BRITE data from 2014, but with better data obtained with BTr in 2016 we have clear evidence for three spots. Despite three more degrees of freedom the credibility gain from a 2-spot model to a 3-spot model is substantial, although the residuals to the model light curves decreased from 1.389 to 1.386 mmag only. In comparison, the clearly noisier data from SMEI (up to a factor of 4) allow only the detection of two spots, which provides again an example for the importance of high quality data.

Bayesian Photometric Imaging routines result in a manifold of solutions. As an example, Figure 4 shows two solutions to the BTr (2016) data: the "barycentric" (top, mean value) and "best fit" (bottom, modal value) solution. They do not coincide satisfyingly, which hints at a serious non-Gaussianity of the posterior as is illustrated in Fig. 2. The most striking difference between the Bayesian Photometric Imaging of the BTr (2016) photometry and the WIRE data set (same Fig. 4) concerns spot latitudes. The marginal distribution of the spot #1 latitude for the BTr data seems to exclude clearly a northern location, contrary to what is determined for the WIRE data. The 'north pole' is defined as the pole which is visible from earth, however, Aithoff projections indicate both poles.

Here, a cautionary note should be heeded: One should keep in mind that the often surprisingly narrow marginal distribution is due to a model's rigidity. It measures its elbowroom – nothing else! If one could relax the rigidity of the model, e.g. by allowing non-circular spots and/or variable contrasts, the marginal distribution would spread out because of the increased freedom! But any additional degrees of freedom came at a price: they would reduce the evidence of a 3-spot model. There is a trade-off between precision of a fit and its credibility. We adhere here to Fermi's rule: better be approximately right than precisely wrong.

– Pulsation: No pulsation is detected in the SMEI data with an amplitude exceeding the detection threshold of 0.33 mmag, corresponding to a S/N = 4.5. The dominant pulsation period, $1/f_1$, derived from red BRITE data agrees exceptionally well with that derived from blue data, but there are significant differences to the pulsation frequencies derived from WIRE and TESS, which will be also subject to a follow-up paper with a detailed asteroseismic analysis (Kallinger et al., in preparation). Anyway, we can improve the pulsation period by combining the times of maximum from BRITE red and WIRE data, resulting in $f_1 = 210.993264(5)\,\mathrm{d}^{-1}$, which, so far, is the most accurately determined f_1 for any roAp star.

The three hitherto well established frequencies, f_1, f_6, and f_7, very likely come from two consecutive radial $l = 0$ modes with an intermediate $l = 1$ mode.

To what extent does a dominant pulsation frequency in the red photometry with an amplitude of, e.g., 0.4 ppt (0.43 mmag) and with a period of 6.8 min contribute to the random noise of a time bin used for spot modelling? In the case of high-precision TESS data and using a time bin of, e.g., 16 min (2.4 times the pulsation period) two-thirds of the variance in such a bin and 9% of the variance of the residuals of our four-spot TESS model can be attributed to oscillation. Hence, we are confident that we did not commit any over-fitting.

– Final Note: The photometric data obtained so-far for α Cir perfectly well illustrate the need for high-precision data on the one hand, *and* long data sets on the other. In general, both qualities are needed for convincing astrophysical analyses, and this fact has to be considered when deciding about investments in ground - as well as in space - based observing technologies.

6. Conclusion

Photometric data obtained for α Cir are discussed concerning stellar variability of the order of days (rotation), down to minutes (pulsation). These data were obtained during individual time slots from 2003 to 2019 with 6 satellites (BRITE-Austria, BRITE-Lem, BRITE-Toronto, WIRE, SMEI, and TESS). The photometric sensitivity of these satellites is different and range from about 400 nm to 900 nm,

At least three surface spots can be identified, which confirms the conclusion of Paper I that a two spot model is too simple. The

present investigation indicates even a fourth spot, but the confirmation is limited due to the relatively poor photometric quality of the blue data, compared to the red one. To our knowledge, this is the first time that the evidence of models differing in the number of spots has been quantitatively determined. Unfortunately, spot latitudes are less well determined than longitudes.

Concerning the main pulsation frequency (f_1) of α Cir, we were able to improve significantly the accuracy (to 0.01 msec) and find indication for a frequency increase from 2014 to 2016, which calls for a separate and focussed investigation including new observations.

The identification of f_1, f_6, and f_7, as two consecutive radial $l = 0$ modes with an intermediate $l = 1$ mode, provide the starting point for an asteroseismic modelling in an upcoming paper.

Acknowledgements. The authors are grateful to Denis Shulyak and Hans Bruntt for providing valuable input to this investigation. Adam Popowicz was supported by Silesian University of Technology, Rector Grant 02/140/RGJ20/0001 (image processing and automation of photometric routines of BRITE-nanosatellite data). AFJM is grateful to NSERC (Canada) for financial aid. The MCMC computations have been performed by HEF at the AIP. This paper includes data collected by the TESS mission, funded by the NASA Explorer Program.

References

Balona, L. A., & Laney, C. D. 2003, MNRAS, 344, 242
Bruntt H. 2007, Communications in Asteroseismology, 150, 326
Bruntt H., & Southworth J. 2008, Journal of Physics Conference Series, 118, 012012
Bruntt, H., North, J. R., Cunha, et al. 2008, MNRAS 386, 2039
Bruntt, H., Kurtz, D. W., Cunha, et al. 2009, MNRAS 396, 1189
Buysschaert B., et al. 2017, A&A, 602, A91
Buzasi D. 2002, in Aerts C., Bedding T. R., Christensen-Dalsgaard J., eds, IAU Colloq. 185: Radial and Nonradial Pulsations as Probes of Stellar Physics, ASP Conf. Series 259, 616
Bychkov, V. D., Bychkova, & L. V., Madej, J. 2005, A&A 430, 114
Cunha M. S., 2006, MNRAS, 365, 153
Feroz, F., Hobson, M. P., & Bridges, M. 2009, MNRAS, 398, 1601
Hubrig, S., Kurtz, D. W., Bagnulo, S., Szeifert, T., Schöller, M., Mathys, G., & Dziembowski, W. A. 2004, et al. A&A 415, 661
Jackson, B. V., Buffington, A., Hick, P. P., et al. 2004, Sol. Phys., 225, 177
Jeffreys H., 1961, Theory of Probability, 3rd edn. Oxford Univ. Press, Oxford
Kallinger, T., Weiss, W. W., Beck, P. G., et al. 2017, A&A 603, 13
Kallinger, T., and Weiss, W. W., 2017, Second BRITE-Constellation Science Conference: Small satellites - big science, Proceedings of the Polish Astronomical Society volume 5, Ed. by K. Zwintz and E. Poretti. Polish Astronomical Society, 113-119
Kallinger, T., Weiss, W. W., Barban, C., et al. 2010, A&A 509, 77
Kallinger, T., Reegen, P., & Weiss, W. W. 2008, A&A, 481, 571
Kochukhov, O., Shulyak, D., & Ryabchikova, T. 2009, A&A 499, 851
Kurtz, D. W., & Balona, L. A. 1984, MNRAS 210. 779
Kurtz, D. W., Martinez, P., & Ashley R. P. 1993, MNRAS 264, 529
Kurtz, D. W., Sullivan, D. J., Martinez, P., & Tripe, P. 1994, MNRAS 280, 1
Landstreet, J. 1980, AJ 85, 611
Lüftinger, Th., Fröhlich, H.-E., Weiss, W. W., et al. 2010, A&A 509, 43
Mathys, G. 1991, A&AS 1991, 89, 121
Mathys, G. 2017, A&A 601, 14
Mathys, G., & Hubrig, S. 1997, A&AS 124, 475
Pablo H., Whittaker, G. N., Popowicz, A., et al. 2016, PASP 128, 970
Pigulski A., et al. 2016, A&A, 588, A55
Popowicz, A. 2016, Proc. SPIE, 9904
Popowicz, A., et al. 2017, A&A, 605, A26
Ricker, G. R., et al. 2015, J. Astron. Telesc. Instr. Syst. 1, 014003
Tarrant, N. J., Chaplin, W. J., Elsworth, Y., Spreckley, S. A., & Stevens, I. R. 2008, A&A 483, 43
Tassoul M. 1980, ApJS, 43, 469
van Leeuwen, F. 2008, A&A 474, 653
Weiss, W. W., & Schneider, H. 1984, A& A, 45, 303
Weiss, W. W., Rucinski, S. M., Moffat, A. F. J., Schwarzenberg-Czerny, A., Koudelka, O. F., et al. 2014, PASP 126, 573
Weiss, W. W., Fröhlich, H.-F., Pigulski, A., Huber, D., Kuschnig, R., Moffat, A.F.J.,Matthews, J. M., Saio, H., Schwarzenberg-Cerny, A., Grant, C. C., Koudelka, O., Lüftinger, Th., Rucincki, S. M., Wade, G. A., Alves, J., Guedel, M., Handler, G., Mochnacki, St., Orleanski, P., Pablo, B., Pamyatnykh, A., Ramiaramanantsoa, T., Rowe, J., Whittaker, G., Zawistowski, T., Zoclonska, E., & Zwintz, K. 2016, A&A 588, 54, **Paper I**
Wood, H. J., & Campusano, L. B. 1975, A&A 45, 303